1   Structurally and functionally distinct early antibody responses predict COVID-19 disease

2   trajectory and mRNA vaccine response

3

4   Saborni Chakraborty[1]†, Joseph C. Gonzalez[1,2]†, Benjamin L. Sievers[3], Vamsee Mallajosyula[4],

5   Srijoni Chakraborty[5], Megha Dubey[6], Usama Ashraf[1], Bowie Yik-Ling Cheng[1], Nimish

6   Kathale[1], Kim Quyen Thi Tran[1], Courtney Scallan[1], Aanika Sinnott[3], Arianna Cassidy[7], Steven T.

7   Chen[8,9,10],Terri Gelbart[3], Fei Gao[4], Yarden Golan[11], Xuhuai Ji[4], Seunghee Kim-Schulze[8], Mary

8   Prahl[12], Stephanie L. Gaw[7], Sacha Gnjatic[9], Thomas U. Marron[8,9], Miriam Merad[8,9,10,13], Prabhu

9   S. Arunachalam[4], Scott D. Boyd[14], Mark M. Davis[4,6,15], Marisa Holubar[1], Chaitan Khosla[16],

10   Holden T. Maecker[4], Yvonne Maldonado[17], Elizabeth D. Mellins[17], Kari C. Nadeau[18], Bali

11   Pulendran[4], Upinder Singh[1,6], Aruna Subramanian[1], Paul J. Utz[19], Robert Sherwood[20], Sheng

12   Zhang[20], Prasanna Jagannathan[1,6], Gene S. Tan[3,21*], Taia T. Wang[1,6,22*]

13

14   [1]Department of Medicine, Division of Infectious Diseases, Stanford University, Stanford, CA,

15   USA.

16   [2]Program in Immunology, Stanford University School of Medicine, Stanford, CA, USA.

17   [3]J. Craig Venter Institute, La Jolla, CA, USA.

18   [4]Institute for Immunity, Transplantation, and Infection, Stanford University School of Medicine,

19   Stanford, CA, USA.

20   [5]Department of Computer and Software Engineering, San Jose State University, San Jose, CA,

21   USA.

22   [6]Department of Microbiology and Immunology, Stanford University School of Medicine,

23   Stanford, CA, USA.

24   [7]Division of Maternal-Fetal Medicine, Department of Obstetrics, Gynecology, and Reproductive

25   Sciences, University of California San Francisco, San Francisco, CA, USA.

26   [8]The Precision Immunology Institute, Icahn School of Medicine at Mount Sinai, New York, NY,

27   USA

28 [9]The Tisch Cancer Institute, Icahn School of Medicine at Mount Sinai, New York, NY, USA

29 [10]Department of Oncological Sciences, Icahn School of Medicine at Mount Sinai, New York,

30 NY, USA

31 [11]Department of Bioengineering and Therapeutic Sciences, and Institute for Human Genetics,

32 University of California San Francisco, San Francisco, CA, USA.

33 [12]Division of Pediatric Infectious Diseases, Department of Pediatrics, University of California,

34 San Francisco, CA, USA.

35 [13]Human Immune Monitoring Center, Precision Immunology Institute, Department of

36 Oncological Sciences, Icahn School of Medicine at Mount Sinai, New York, NY, USA.

37 [14]Departments of Pathology and of Microbiology and Immunology, Stanford University School

38 of Medicine, Stanford, CA, USA.

39 [15]Howard Hughes Medical Institute, Stanford University School of Medicine, Stanford, CA

40 94305, USA.

41 [16]Departments of Chemistry and Chemical Engineering, Stanford University, Stanford, CA,

42 USA.

43 [17]Department of Pediatrics, Stanford University School of Medicine, Stanford, CA, USA.

44 [18]Sean N. Parker Center for Allergy and Asthma Research, Stanford, CA, USA.

45 [19]Department of Medicine, Division of Immunology and Rheumatology, Stanford University
46 School of Medicine, Stanford, CA, USA
47 [20]Proteomics and Metabolomics Facility, Institute of Biotechnology, Cornell University, Ithaca,

48 NY, USA.

49 [21]Division of Infectious Diseases, Department of Medicine, University of California San Diego,

50 La Jolla, CA, USA.

51 [22]Chan Zuckerberg Biohub, San Francisco, CA, USA.

52

53 † these authors contributed equally

54 [*] these authors contributed equally

55 Corresponding author: taiawang@stanford.edu

56

57

58

59

60

61   Abstract

62   A damaging inflammatory response is strongly implicated in the pathogenesis of severe COVID-

63   19 but mechanisms contributing to this response are unclear. In two prospective cohorts, early

64   non-neutralizing, afucosylated, anti-SARS-CoV-2 IgG predicted progression from mild, to more

65   severe COVID-19. In contrast to the antibody structures that predicted disease progression,

66   antibodies that were elicited by mRNA SARS-CoV-2 vaccines were low in Fc afucosylation and

67   enriched in sialylation, both modifications that reduce the inflammatory potential of IgG. To

68   study the biology afucosylated IgG immune complexes, we developed an *in vivo* model which

69   revealed that human IgG-FcγR interactions can regulate inflammation in the lung. Afucosylated

70   IgG immune complexes induced inflammatory cytokine production and robust infiltration of the

71   lung by immune cells. By contrast, vaccine elicited IgG did not promote an inflammatory lung

72   response. Here, we show that IgG-FcγR interactions can regulate inflammation in the lung and

73   define distinct lung activities associated with the IgG that predict severe COVID-19 and

74   protection against SARS-CoV-2.

75

76   One Sentence Summary: Divergent early antibody responses predict COVID-19 disease

77   trajectory and mRNA vaccine response and are functionally distinct *in vivo.*

78

79   The minority of people who develop severe COVID-19 during SARS-CoV-2 infection mount an

80   inflammatory response that is strongly implicated in disease pathogenesis (*1-3*). The extreme

81   inflammatory phenotype in the lungs of severe COVID-19 patients is clear from autopsy studies,

82   but mechanisms contributing to this response are not well understood (*4-7*). IgG antibodies

83 mediate cellular functions that are central in directing the course of disease during many viral

84 infections. Aside from neutralizing activity, IgG antibodies that bind to virus particles or viral

85 antigens can form immune complexes (ICs) that may have a profound impact on disease

86 pathogenesis, especially with regard to inflammation. This is observed in some autoimmune and

87 infectious diseases where persistent ICs drive a hyperinflammatory response that damages host

88 tissues (*8*). A clear mechanism underlying modulation of inflammation by antibodies is via IgG

89 interactions with activating and inhibitory Fc gamma receptors (FcγRs) on myeloid cells, which

90 are central regulators of the inflammatory response. We and others have previously found that

91 patients with severe COVID-19 produce a high level of afucosylated IgG antibodies that trigger

92 inflammatory responses in primary monocytes (*9-11*). This response was dependent on Fc

93 afucosylation, a modification that enhances affinity of monomeric IgG for the activating FcγR,

94 CD16a, by approximately 10-fold (*12, 13*).

95

96 Because IgG ICs can promote disease sequelae in some infections, the link between severe

97 COVID-19 and afucosylated IgG suggests that this antibody type may have a role in the

98 inflammatory pathogenesis of severe disease. To explore this, we first studied whether

99 afucosylated antibody production was a consequence of, or an antecedent to, the development of

100 more severe COVID-19. In two independent cohorts, assessed during an initial period of mild

101 symptoms, we found that the absence of early neutralizing antibodies, together with an increased

102 abundance of afucosylated IgG, predicted rapid progression to more severe disease. Elevated

103 frequencies of monocytes expressing the receptor for afucosylated IgG, CD16a, also predicted

104 more severe outcomes. To study the effect of afucosylated antibody signaling in the lungs, we

105 developed a novel model system in which human ICs of defined composition are intratracheally

106 administered to mice that express human FcγRs (*14*). Molecular and cellular changes that were

107 triggered in the lung by distinct antibody signaling pathways can then be assessed by

108 characterization of broncho alveolar lavage (BAL) fluid collected after IC administration. This

109 model provides a physiologically relevant system to study antibody effector responses in the

110   lung. We observed that afucosylated ICs triggered robust immune cell activation, infiltration into

111   the lungs, and proinflammatory cytokine production that was CD16a-dependent. In contrast to

112   natural infection, SARS-CoV-2 mRNA vaccination elicited IgG antibodies that were both highly

113   fucosylated and sialylated. Immune complexes formed from the mRNA vaccine-elicited IgG did

114   not trigger the cellular infiltration and the cytokines/chemokines that were associated with

115   afucosylated IgG *in vivo*. Overall, these findings demonstrate that early production of non-

116   neutralizing, afucosylated IgG1 was predictive of COVID-19 symptom progression; these

117   antibodies were structurally and functionally distinct from IgG1 elicited by mRNA SARS-CoV-2

118   vaccination.
119

120

121   Results

122   Study cohorts

123   To study the early antibody features that correlated with different disease outcomes in COVID-

124   19, we characterized IgG from two longitudinal cohorts of COVID-19 outpatients from Stanford

125   Hospital Center (n=109 Cohort 1 at enrollment; n=69 Cohort 2). While these samples were

126   collected from interventional clinical studies, we present data only from the placebo arm of both

127   studies; thus, our findings are not impacted by the experimental treatments trialed in either study.

128   Participants in both studies were enrolled early in infection, within three days of a positive

129   SARS-CoV-2 PCR test. All subjects presented with mild COVID-19 and had mild symptoms at

130   the time of enrollment, as determined by a physicians assessment (*15*). While uncomplicated

131   resolution of mild disease occurred in the majority of subjects, a subset of patients in each cohort

132   (n=8 in Cohort 1; n=7 in Cohort 2) developed worsening symptoms in the hours or days

133   following enrollment. These subjects were evaluated in the emergency department and some

134   required hospitalization; one subject succumbed to disease. We term these patients with distinct

135   disease trajectories as "progressors" (Tables S1, S2, S3) or "non-progressors". Progressors and

136   non-progressors from Cohort 1 did not significantly differ by the parameters of age, weight, or

137   sex. Progressors from Cohort 2 also did not differ based on weight or sex but were older

138   compared to non-progressors (Table S1).

139

140   Low early neutralizing IgG levels in progressors

141   The availability of samples from the date of enrollment in both studies (here termed "day 0"),

142   when all subjects had mild disease, enabled our analysis of early antibody responses that

143   correlated with distinct disease trajectories. We first defined the evolution of the neutralizing

144   antibody response following SARS-CoV-2 infections using a pseudotyped vesicular stomatitis

145   virus neutralization assay. The fifty percent pseudoviral neutralizing antibody titers (pNT_{50}) were

146   calculated for day 0, day 5, day 28, month 7, and month 10 for all subjects in the placebo arm of

147   Cohort 1 from whom samples were available. Samples from study participants who received a

148   SARS-CoV-2 vaccine within the study period were not evaluated. In most subjects, levels of

149   neutralizing antibodies showed a significant increase over time, peaking by day 28. Once

150   initiated, the antibody response was durable and persisted in most people until 7 months post-

151   enrollment, after which there was a general decrease in neutralization by month 10 (Fig. 1A,

152   S1A). This analysis of Cohort 1 revealed that although there was considerable heterogeneity in

153   early neutralizing responses, those participants who would progress to more severe disease had

154   uniformly very low or no detectible neutralizing antibodies at the study day 0/enrollment time

155   point (Fig. 1B). Cohort 2 showed somewhat less heterogeneity in early neutralizing responses,

156   but as with Cohort 1, neutralizing antibodies were not detected on day 0 in any of the progressors

157   (Fig. 1B). These data were broadly consistent with studies showing a correlation between early

158   neutralizing antibody responses and outcomes in COVID-19 (*16-19*).

159

160   We initially reasoned that the absence of early neutralizing antibodies in progressors might have

161   been due to earlier sampling of participants who were on a more severe disease trajectory. To

162   evaluate this, we compared the number of symptomatic days prior to study enrollment in

163   progressors and non-progressors. This revealed that there was no significant difference in the

164   mean or median duration of symptoms prior to enrollment (Table S1). Thus, the kinetics of

165   sampling did not explain this observation. Despite the absence of early neutralizing responses,

166   SARS-CoV-2 spike-reactive IgG was clearly present in all progressors (Fig. 1C). While early

167   neutralizing responses were not detected, progressors from whom longitudinal samples were

168   available generally mounted neutralizing antibody responses by the later study timepoints (Fig.

169   S1B).

170

171   Elevated early production of afucosylated IgG in progressors

172   We next asked whether there were qualitative differences in the Fc structures of the IgG in

173   progressors and non-progressors. As we had previously observed elevated anti-SARS-CoV-2 Fc

174   afucosylation in hospitalized patients compared to outpatients (*9*), we sought to clarify whether

175   these antibodies were produced in response to severe disease or whether they might precede the

176   development of severe symptoms. To study this, we evaluated Fc glycosylation on antibodies

177   present at study enrollment when all subjects had mild symptoms. Indeed, at study enrollment

178   the progressors in both cohorts were already distinguished by elevated levels of afucosylated

179   IgG1, comparable to the levels observed in a cohort of hospitalized COVID-19 patients in the

180   Mount Sinai Health System (Fig. 1D, E, Table S1) (*20*). The abundance of afucosylated IgG1 in

181   COVID-19 outpatients was not different across timepoints that were separated by approximately

182   200 days (Fig. S1C). These data show that production of afucosylated IgG preceded the onset of

183   severe symptoms and afucosylated antibodies were maintained over time.

184

185   We next sought to investigate the basis of differences in antibody fucosylation. We hypothesized

186   that differences in expression of the relevant glycosyltransferase, α-1,6-fucosyltransferase

187   (FUT8), by antibody-secreting cells, might play a role. To investigate this, we assessed FUT8

188   protein levels in peripheral blood mononuclear cells (PBMCs) from progressors and non-

189   progressors (Fig. S2A). At the time of this experiment, only PBMCs from Cohort 2 were

190   available from the enrollment timepoint. Because we have previously observed a sex-based

191   difference in antibody afucosylation (*9*), an equivalent number of sex-matched non-progressors

192   were selected for this analysis. We observed no other correlations between demographic features

193   and IgG afucosylation in either cohort (Fig. S1D). Consistent with the elevated production of

194   afucosylated IgG by progressors, CD19+ B cells and plasmablasts from progressors expressed

195   less FUT8 than cells from non-progressors upon enrollment (Fig. 1F). FUT8 expression within

196   total PBMCs was comparable between groups, as was the distribution of B cell subsets,

197   suggesting that FUT8 expression is regulated at the effector cell level (Fig. S2A, S2B, S2C). Of

198   note, plasmablast expression of FUT8 correlated with IgG1 Fc afucosylation, supporting the

199   hypothesis that IgG afucosylation is regulated at least in part by the expression level of FUT8

200   (Fig. 1G).

201

202   Early non-neutralizing, afucosylated anti-spike IgG predict worsening symptoms in COVID-19

203   outpatients

204   To determine whether the combination of low/no neutralizing antibodies and elevated IgG Fc

205   afucosylation was a predictor of worsening disease trajectory in mild COVID-19 patients, we

206   next trained and evaluated a logistic regression model by using day 0 neutralization titers and

207   afucosylated IgG frequency as input features from Cohort 1. Individually, both early

208   neutralization titers and Fc afucosylation had low to modest predictive power to separate

209   progressors and non-progressors, while combining the two features could separate progressors

210   from non-progressors with higher predictive accuracy (Fig. 1H). Subsequently, the Cohort 1 data

211   was used as the training set and the performance of the model was evaluated on an independent

212   test dataset (Cohort 2). As shown, the combined features could discriminate divergent disease

213   outcomes with area under the receiver operating characteristic (ROC) curve (AUC) of 0.81 (Fig.

214   1I). Thus, early production of reactive, afucosylated antibodies and poor serum neutralizing

215   activity predicted progression from mild COVID-19 to more severe outcomes.

216

217

218
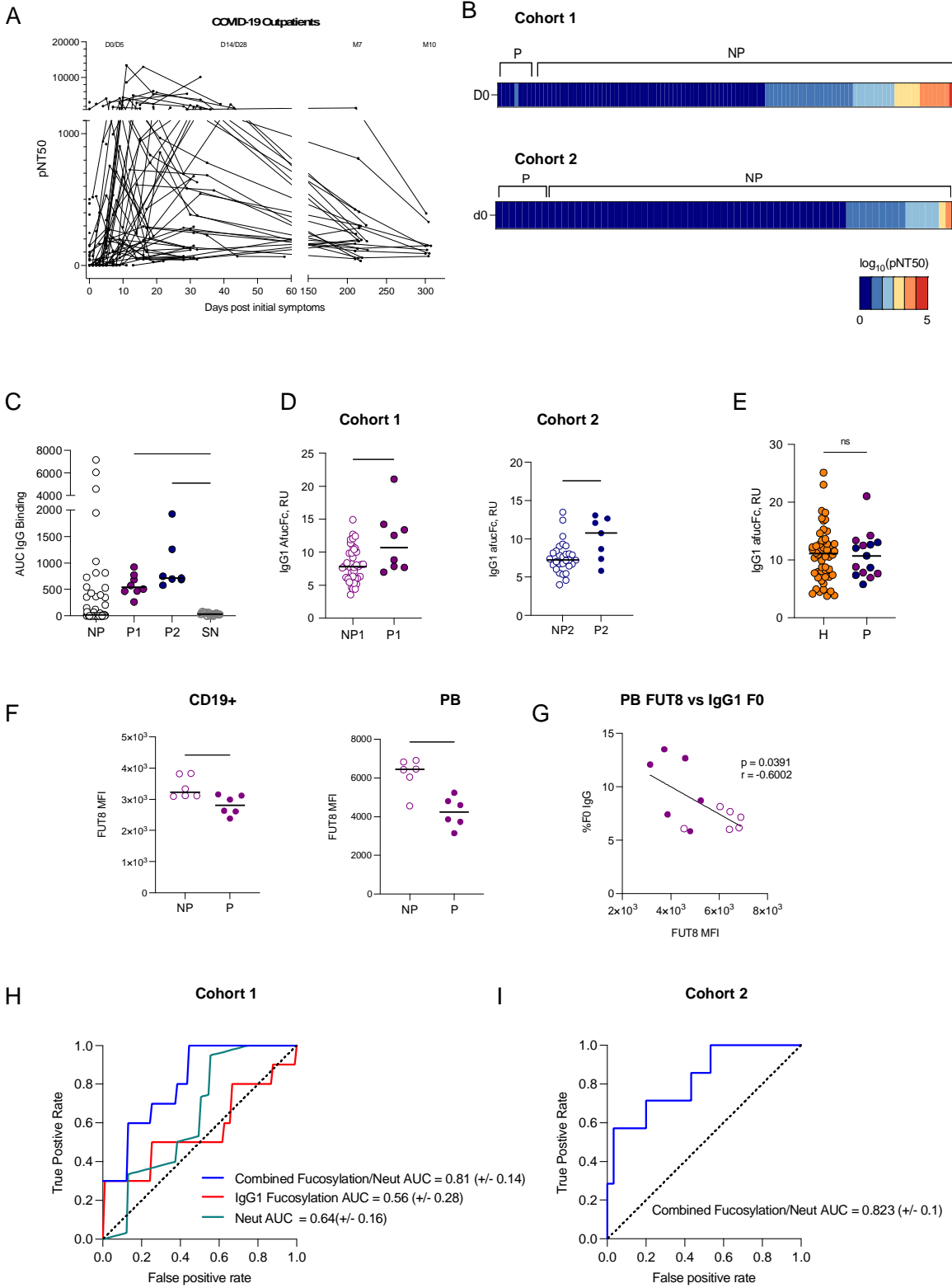
Figure 1. Low early neutralizing titers and elevated Fc afucosylation predict disease progression.
(A) The kinetics of neutralizing antibody response over time in Cohort 1. Half-maximal SARS-CoV-2 pseudovirus neutralizing titers (pNT_{50}) at each study time point, graphed based on days of symptoms for each participant. Samples were collected at study day 0 (D0 enrollment; n=101), 5 (D5; n=50), 14 (D14; n=33), 28 (D28; n=43), month 7 (M7; n=24) and month 10 (M10; n=9). **(B)** Heatmap of pNT_{50} data in progressors (P) (Cohort 1 n=8, Cohort 2 n=7) and non-progressors (NP) at enrollment timepoint (D0). **(C)** SARS-CoV-2 spike-binding IgG (AUC) of Cohort 1 progressors (P1, solid purple), Cohort 2 progressors (P2, solid blue), random subset of non-progressors, and historic seronegative (SN) sera. **(D)** IgG1 Fc afucosylation levels of progressors and non-progressors at enrollment timepoint (D0) of Cohort 1 (purple; progressors=P1, non-progressors=NP1), Cohort 2 progressors (blue; progressors=P2, non-progressors=NP2). **(E)** IgG1 Fc afucosylation levels in COVID-19 patients who were hospitalized (H, orange) (n=52) and combined outpatient progressors (P, Cohort 1 progressors: purple), Cohort 2 progressors: blue) (n=15). **(F)** α-1,6-Fucosyltransferase 8 (FUT8) median fluorescence intensity in total CD19+ B cells and in plasmablasts (PB) from progressors (n=6) relative to sex-matched non-progressors (n=6). **(G)** Correlation in matched samples: plasmablast expression of FUT8 and the abundance of IgG1 afucosylation. Solid and open circles represent data points from progressors and non-progressors, respectively. **(H)** Mean receiver operating characteristic (ROC) response and the area under the curve (AUC) with its standard deviation obtained using a logistic regression model using neutralization titers and IgG1 afucosylation levels. **(I)** Receiver operating characteristic (ROC) response and the area under the curve (AUC) with standard deviation obtained by testing logistic regression model on an independent Cohort 2. Median values are depicted in C-F with a solid black line. P values in (C) were calculated using Brown-Forsythe and Welch ANOVA test with Dunnett T3 correction, in (D-E) were calculated using Wilcoxon rank-sum test and in (F) using unpaired Student's test. *P < 0.05; **P < 0.01; ***P < 0.001; ****P < 0.0001. Pearson's correlation coefficient (r = -0.6002, p = 0.0391,) was computed in (G).

219

220   The receptor for afucosylated IgG1, CD16a, is enriched in the myeloid compartment of

221   progressors

222   In addition to afucosylated antibody production, a hallmark of patients with severe COVID-19 is

223   inflammatory myeloid cell infiltration into the lung and excessive inflammatory cytokine

224   production (*2, 21, 22*). These cells express the low affinity FcγRs CD32a (activating), CD32b

225   (inhibitory) and, on some subsets, CD16a (activating). These low affinity FcγRs are engaged

226 through avidity-based interactions when ICs are formed during infection. Depending on the

227 magnitude of activating or inhibitory signal received upon engagement, an effector cell will

228 respond with a proportional level of inflammatory activity (*9*). Considering that severe COVID-

229 19 is often characterized by an aberrant effector cell activation state (*1, 23-25*), we next sought to

230 define the expression of activating and inhibitory FcγRs on peripheral monocytes from

231 progressors and non-progressors that might counterbalance or compound an enrichment of

232 afucosylated IgG.

233

234 To study this, available PBMC samples collected at study enrollment were assessed for the

235 frequency of CD16a-expressing monocyte subsets as well as their expression of all low affinity

236 FcγRs (Fig. S3A). Notably, we found that progressors had significantly increased frequencies of

237 total CD16a+ monocytes, CD16a+ CD14- non-classical monocytes, and CD16a+ CD14+

238 intermediate monocytes within the peripheral CD11c+ HLA-DR+ myeloid cell compartment

239 compared to non-progressors upon study enrollment (Fig. 2A) (*26-28*). Further, quantitative

240 expression analysis of CD16a within these immune cell subsets revealed higher levels of CD16a

241 on cells from progressors, while other low affinity FcγRs (CD32a/b) were not differentially

242 expressed (Fig. 2B, Fig. S3B). Taken together, early CD16a expression within the peripheral

243 myeloid cell compartment predicted the development of more severe symptoms in COVID-19

244 outpatients (Fig. 2C,D).
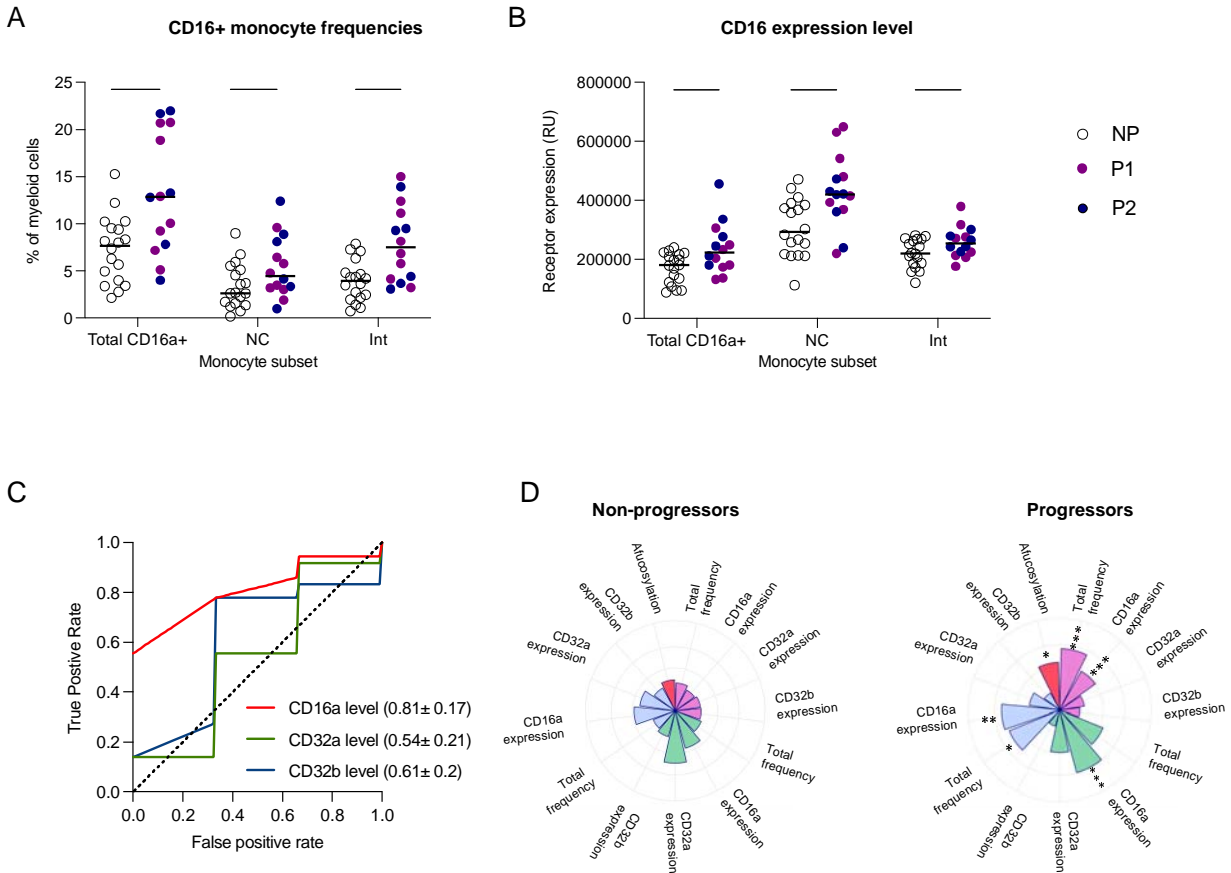
245

Figure 2. Elevated CD16a signaling potential in myeloid compartment in progressors. Enrollment time point PBMCs were characterized in progressors (n=14) and a randomly selected subset of non-progressors (n=18). Solid purple and blue circles represent data points from progressors within Cohort 1 and Cohort 2, respectively whereas open circles represent data points from non-progressors. The median values have been depicted with a black line. **(A)** Total CD16a+ monocyte, CD16a+ CD14- non-classical monocyte (NC), and CD16a+ CD14+ intermediate monocyte (Int) frequencies as percents of total CD11c+ HLA-DR+ CD3- CD19- CD56- myeloid cells are shown. **(B)** CD16a expression levels on total CD16a+, non-classical, and intermediate monocyte populations. **(C)** Mean ROC response and the area under the curve (AUC) with its standard deviation obtained using random forest classifier with 6-fold cross validation in 2 outpatient cohorts using FcγR expression levels on myeloid cells. **(D)** Radar plots summarizing the various features of IgG1-CD16a signaling axis in progressors and non-progressors. Significant differences between the two groups are indicated with asterisks in the radar plot for progressors. P values in (A-B) were calculated using unpaired t-tests. (*P < .05, **P < .01, ***P < .001, ****P < 0.0001).

246

247   mRNA vaccination elicits the production of neutralizing IgG with glycoforms that are distinct

248   from those elicited by infection

249   We next sought to compare the quality of antibodies produced after SARS-CoV-2 mRNA

250   vaccination and infection. To do so, we studied the antibodies elicited after 1 and 2 doses of the

251   Pfizer BNT162b2 SARS-CoV-2 mRNA vaccine in a group of healthy SARS-CoV-2-naïve adults

252   (Stanford adult vaccine cohort, n=29) (Table S4). Neutralizing titers increased between the post-

253   primary vaccination timepoint (21 days post-dose 1 (PD1)) and the post-boost timepoint (21 days

254   post-dose 2 (PD2)). In all, two doses of mRNA SARS-CoV-2 vaccine elicited robust neutralizing

255   antibody responses that were elevated over peak outpatient neutralizing titers (day 28 shown)

256   (Fig. 3A). Over time after vaccination, the distribution of anti-spike IgG subclasses shifted to a

257   more dominant proportion of IgG1 antibodies (Fig. 3B).

258

259   We next characterized Fc glycoforms of anti-spike IgG to determine whether infection- and

260   mRNA vaccine-elicited IgG were distinct in this respect (*10*). For this analysis, IgG from day 28

261   of the outpatient COVID-19 study (from non-progressors) were compared to samples drawn

262   from vaccine recipients on day 28 post-primary vaccination (7 days post-boost). Additionally, we

263   compared these groups to IgG from the hospitalized COVID-19 cohort (Mount Sinai). Levels of

264   IgG1 Fc afucosylation were similar between the outpatient and vaccine-elicited IgG (Fig. 3C)

265   and both groups were significantly reduced in afucosylation relative to hospitalized patients.

266   Interestingly, vaccination-induced IgG was significantly enriched in Fc sialylation over both

267   outpatient and hospitalized COVID-19, suggesting differential regulation of Fc sialylation by

268   mRNA vaccination and infection, though we cannot exclude a contribution from demographic

269   features that were not matched between cohorts. The relative homogeneity of Fc glycosylation in

270   response to mRNA vaccination contrasted with the heterogeneity observed in natural infection,

271   as well as with our previous observations after seasonal influenza virus vaccination, suggesting

272   differences in the response that may be based on the context of antigen encounter, antigen

273   experience, or different vaccine platforms (*29*). Vaccine-elicited Fc afucosylation and sialylation

274   were relatively stable over time, similar to the stability observed after natural infection (Fig. 3D,

275   Fig. S1C). Thus, SARS-CoV-2 infection and mRNA vaccination both elicited high neutralizing

276   titers, but distinct and stable levels of IgG1 Fc afucosylation and sialylation.
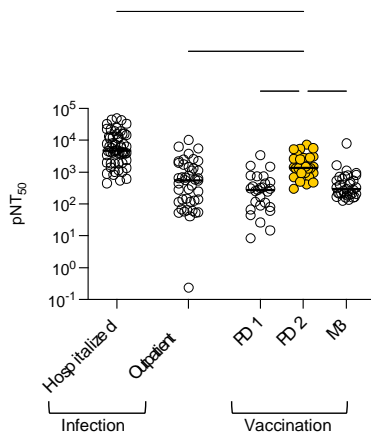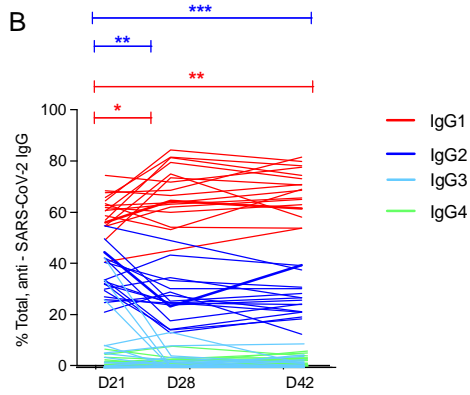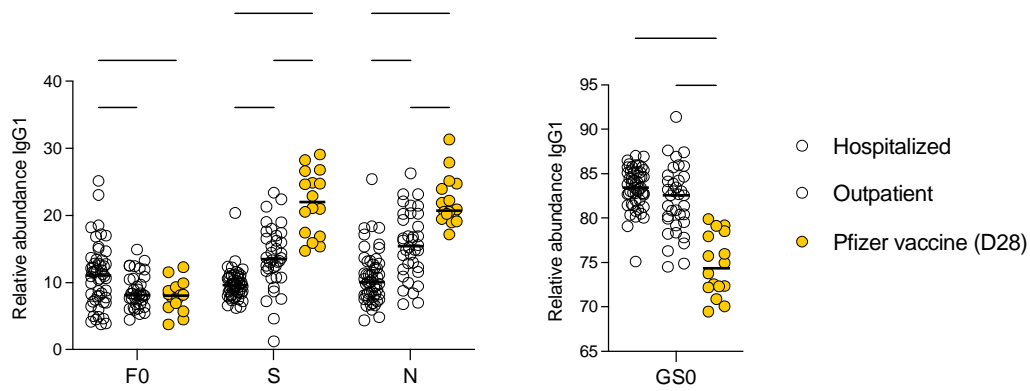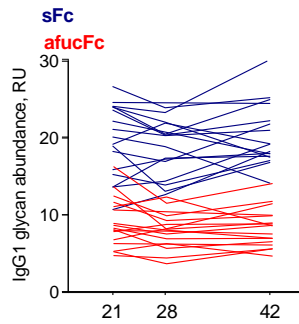
277

278

Figure 3. mRNA vaccination elicits high neutralizing antibody titers with Fc glycoforms distinct from both infection-induced phenotypes. (A) The half-maximal SARS-CoV-2 pseudovirus neutralizing titers (pNT_{50}) in healthy adults following mRNA vaccination (yellow n=29) or in COVID-19 outpatients on study day 28 (blue n=42). PD1: post-dose 1, PD2: post-dose 2, M3: month 3. **(B)** Longitudinal analysis of IgG subclasses on day 21, 28 or 42 post-primary vaccination (n=17). **(C)** SARS-CoV2 IgG1 Fc posttranslational modifications in hospitalized COVID-19 patients (n=52), COVID-19 outpatients (day 28 n=36) and in subjects who received the mRNA SARS-CoV-2 vaccine (day 28 post primary vaccination, n=17). F0: afucosylation, S: sialylation, N: bisection, GS0: galactosylation. The median values have been depicted with a black line. **(D)** Longitudinal analysis of anti-SARS-CoV-2 IgG1 Fc afucosylation (afucFc, red line) and sialylation (sFc, blue line) on day 21, 28 or 42 post-primary vaccination. P values in (A) were calculated using Kruskal Wallis test with Dunn's correction, (B) using mixed effect analysis with Geissser-Greenhouse and Tukey's corrections, (C) two-way ANOVA and one-way ANOVA with Tukey's correction. *P < 0.05; **P < 0.01; ***P < 0.001; ****P < 0.0001.

279

280

281 Afucosylated immune complexes trigger inflammation in the lung *in vivo*

282 To study the functional relevance of the differential glycosylation of mRNA- and infection-

283 elicited IgG, we established an *in vivo* experimental model designed specifically to enable

284 dissection of human antibody signaling outcomes in the lung, in the absence of any additional

285 effects imposed by infection. In this model, pre-formed human IgG ICs, simulating what would

286 be formed during an infection, are delivered to lungs of mice that express human, instead of

287 murine, FcγRs, with cell-specific distribution that mimics the human system (*14*). Polyclonal

288 IgG pools were generated from purified serum IgG. Pools were from patients with elevated (pool

289 1, >20%) or normal levels (pool 2, <10%) of afucosylated IgG or from sera of mRNA-vaccinated

290 adults (pool 3). Pools 1 and 2 did not significantly differ in other glycan modifications, and all 3

291 pools exhibited comparable distribution of IgG subclasses, though we acknowledge that pool 3

292   trends toward a lower IgG1 and higher IgG2 content (Fig. S4A, S4B). All IgG pools were

293   standardized for binding to SARS-CoV-2 spike (Fig. S4C). Mice were intratracheally

294   administered ICs composed of the anti-SARS-CoV-2 IgG and trimeric SARS-CoV-2 spike

295   protein. Four hours following IC administration, contents of BAL fluid were analyzed for

296   immune cells and soluble factors. This system provided a context in which to specifically study

297   how modulation of IgG Fc-FcγR interactions impacts the immune response in the lung.

298

299   BAL fluid collected from the lungs of mice that were treated with afucosylated ICs (pool 1) had

300   significantly elevated frequencies of neutrophils and monocytes over BAL fluid from mice

301   treated with fucosylated ICs (pool 2) or mRNA-vaccine elicited ICs (pool 3) (Fig. 4A, Fig. S5).

302   BAL fluid from mice that received afucosylated ICs was also distinguished from all other

303   experimental conditions by increased concentrations of proinflammatory cytokines and

304   chemokines. TNFα, IL-6, CCL3, CCL4, CXCL1, and CXCL10 were significantly and uniquely

305   upregulated while no difference was observed in levels of the immunoregulatory or

306   immunosuppressive cytokine IL-10 (Fig. 4B). Collectively, these findings functionally

307   distinguish afucosylated IgG, characteristic of severe COVID-19, from the highly sialylated and

308   fucosylated, vaccine-elicited antibody glycoforms *in vivo*.

309

310   We next assessed the FcγR dependence of the immune response to afucosylated ICs. Mice

311   specifically lacking expression of CD16a (CD16a-/-), but expressing all other human FcγRs, did

312   not exhibit a similar inflammatory response to afucosylated ICs as mice expressing the complete

313   human repertoire (WT) (Fig. 4C, D). This showed that the inflammatory potential of

314   afucosylated IgG1 was almost entirely dependent on the presence of CD16a-expressing immune

315   effector cells. Because CXCL1 and CCL3 are known neutrophil chemoattractants, we next asked

316   whether these molecules mediated the neutrophil influx after afucosylated IC administration.

317   Indeed, pre-administration of blocking monoclonal antibodies against the chemokines CXCL1 or

318   CCL3 led to a significant reduction in neutrophil recruitment (Fig. 4E) (*30, 31*). Together, these

319   findings support a mechanism in which afucosylated ICs in the lung trigger CD16a-dependent

320   production of chemokines which promote subsequent influx of innate immune cells.

321
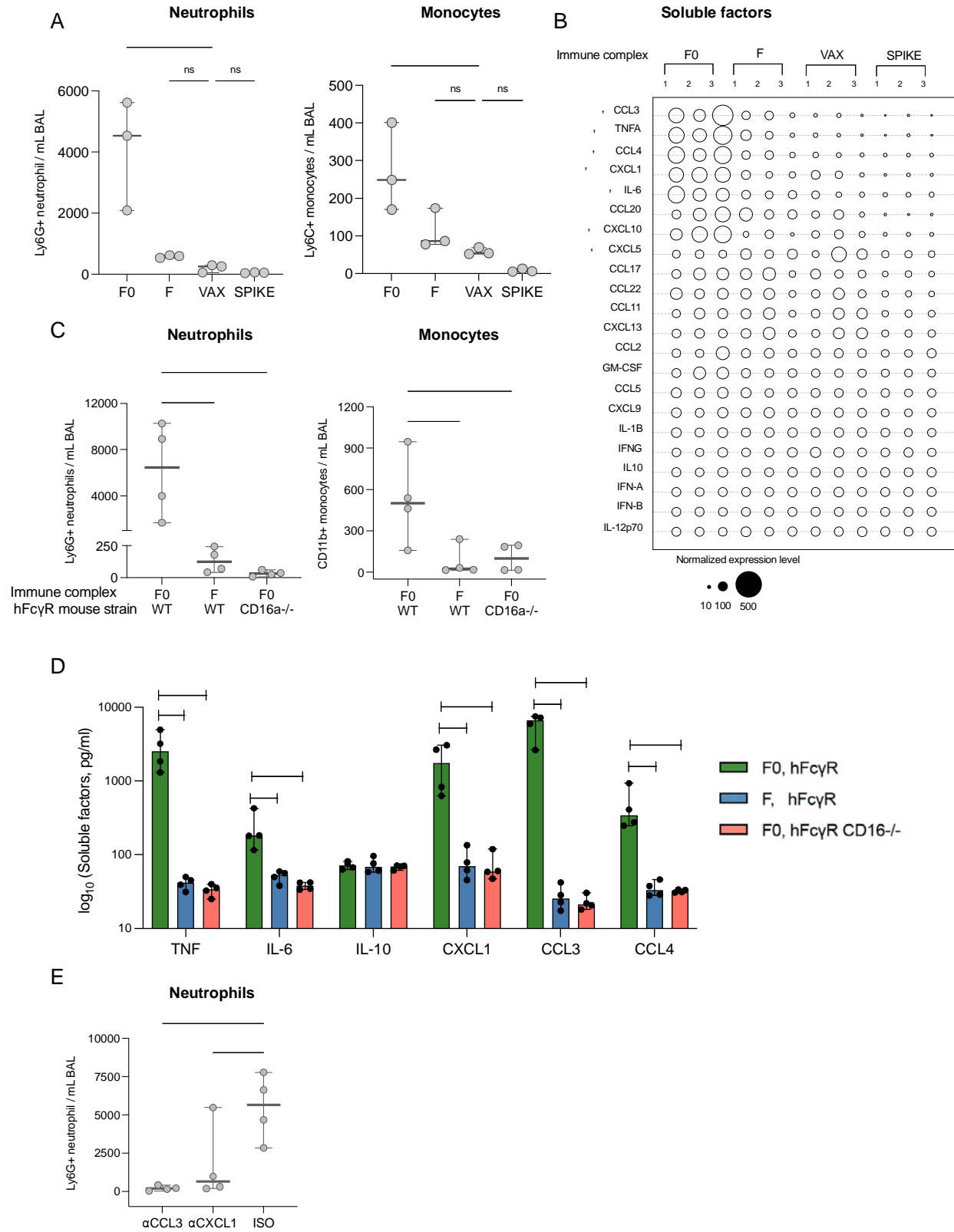
Figure 4. Afucosylated IgG immune complexes promote cell infiltration and proinflammatory cytokine production *in vivo*. **(A)** Immune cells measured in the bronchoalveolar lavage (BAL) fluid of human Fcγ receptor mice (hFcγR) that were treated with either afucosylated (F0, pool 1), normally fucosylated (F, pool 2), vaccine-induced (VAX, pool 3) immune complexes or spike alone, by intratracheal administration. **(B)** Cytokine/chemokine levels in the BAL of the various groups of mice. The size of the bubble represents normalized cytokine and chemokine levels. p values are indicated for each soluble factor (blue: F0 vs F, red: F0 vs VAX). **(C)** Immune cell subsets, **(D)** cytokines (TNF, IL-6, IL-10) and chemokines (CXCL1, CCL3, CCL4) quantitated in the bronchoalveolar lavage (BAL) fluid of hFcγR or hFcγR mice with a specific deletion in CD16a (CD16a-/-) that received afucosylated (F0, pool 1) or normally fucosylated (F, pool 2) immune complexes by intratracheal administration. In **(A)** and **(C)** neutrophils were defined as Ly6G+ CD11b+ CD2- CD3- B220- cells and total monocytes defined as CD11b+ Ly6G- MERTK- MHC IA/IE- CD2- CD3- B220- cells. **(E)** Frequency of Ly6G+ CD11b+ CD2- CD3- B220- neutrophils in BAL fluid of hFcγR mice that were pre-treated with chemokine neutralizing mAbs (αCXCL1 and αCCL3) or isotype control followed by administration of afucosylated immune complexes. The median and the 95% confidence interval have been depicted in each graph with solid lines. P values in (A-D) were calculated using one-way ANOVA with Dunnett's correction using n=3 mice per group for A and B and n=4 mice per group for C-E. Data in A-E are representative of at least two independent experiments. *P < 0.05; **P < 0.01; ***P < 0.001; ****P < 0.0001.

322

323   Discussion

324   Prognostic biomarkers and treatments that may halt the progression to severe COVID-19 are

325   urgently needed to prevent mortality associated with this disease. To identify new avenues of

326   treatment, mechanisms underlying the distinct trajectories in COVID-19 must be clarified. Here,

327   we show that early antibody quality and the expression of cognate FcγRs on peripheral

328   monocytes may be used to anticipate distinct COVID-19 trajectories, including progression to

329   more severe outcomes. Overall, mild COVID-19 patients who experienced a worsening disease

330   trajectory were characterized by the absence of an early robust neutralizing antibody response

331   with elevations in both afucosylated anti-spike IgG and the CD16a receptor on myeloid cells.

332   The IgG elicited by SARS-CoV-2 infection was heterogenous in Fc glycosylation relative to IgG

333   generated in response to SARS-CoV-2 mRNA vaccination. Vaccine-elicited IgG exhibited high

334   neutralization and low afucosylation, along with other significant differences in Fc glycoforms.

335   The early inflammatory response to ICs in the lung was a function of the abundance of IgG1

336   afucosylation and CD16 expression.

337

338   Our data support a model in which the combination of a lack of early SARS-CoV-2

339   neutralization and an enhanced afucosylated IgG-CD16a signaling axis contribute to the

340   inflammatory phenotype of severe COVID-19. We propose that this may be one mechanism

341   contributing to the hyperinflammatory response in severe COVID-19. Determining how various

342   immune aberrancies, including those described here and others such as elevated IL-6 or an

343   impaired renin-angiotensin system might contribute to the pathogenesis of severe COVID-19

344   will require the development of new animal models (*2, 24, 32, 33*). To examine whether

345   afucosylated ICs can augment the inflammatory milieu in the lungs, we established a model to

346   specifically evaluate the impact of human IgG signaling on the pulmonary inflammatory

347   response. This model advances our ability to evaluate human IgG antibodies in a functional

348   dimension, beyond what *in vitro* approaches can reveal. We show that the afucosylated

349   IgG/CD16a signaling axis can result in a complete remodeling of the inflammatory lung milieu.

350   Of note, the increased frequency of neutrophils and monocytes observed within the lungs of mice

351   that received afucosylated ICs mirrors what has been observed in some severe COVID-19

352   patients (*4, 21, 34, 35*). Tissue-resident alveolar macrophages likely serve as an initial effector of

353   afucosylated IC activity in this model as they are the predominant innate immune cell population

354   within the lung, express high levels of CD16a, and can produce many of the observed soluble

355   factors (*11*). This *in vivo* model is not a model of COVID-19 pathogenesis; rather, it enables a

356   more targeted investigation of how distinct human antibody repertoires activate effector cells and

357   the complex molecular changes involved in those interactions specifically within the lung.

358   Animal models that more accurately reflect the immunophenotype of patients at highest risk for

359   mortality in COVID-19 are needed to truly study the pathogenesis of this disease.

360

361   While we did not observe a significant correlation between IgG afucosylation and the

362   demographic features studied here, it is known that IgG post-translational modifications are

363   associated with specific patient characteristics including sex and age (*36*). Thus, differences in

364   demographics between our cohorts may have contributed to our findings. How IgG glycosylation

365   is regulated is not fully understood, but numerous studies support a role for both heritable and

366   non-heritable influences (*29, 37-41*). We believe that the data in our current manuscript are the

367   first to support a direct role for plasmablast FUT8 expression as a determinant of IgG

368   afucosylation. Defining specific regulatory pathways of IgG glycosylation will be important for

369   modulating the *in vivo* activities of IgG to improve human disease outcomes.

370

371

372

373

374

375

376   Materials and Methods

377

378   Clinical cohorts and samples

379   Characterization of these samples at Stanford was performed under a protocol approved by the

380   Institutional Review Board of Stanford University (protocol #55718).

381   Stanford Lambda cohort (Cohort 1):

382   120 participants were enrolled in a phase 2 randomized controlled trial of Peginterferon Lambda-

383   1a beginning April 25, 2020 (Lambda, NCT04331899). Inclusion/exclusion criteria and the study

384   protocol for the trial have been published(*15*). Briefly, adults aged 18-75 years with an FDA

385   emergency use authorized reverse transcription-polymerase chain reaction (RT-PCR) positive for

386   SARS-CoV-2 within 72 hours prior to enrollment were eligible for study participation. Exclusion

387   criteria included hospitalization, respiratory rate >20 breaths per minute, room air oxygen

388   saturation <94%, pregnancy or breastfeeding, decompensated liver disease, recent use of

389   investigational and/or immunomodulatory agents for treatment of COVID-19, and prespecified

390   lab abnormalities. All participants gave written informed consent, and all study procedures were

391   approved by the Institutional Review Board of Stanford University (IRB-55619). Participants

392   were randomized to receive a single subcutaneous injection of Lambda or saline placebo.

393   Peripheral blood was collected at enrollment, day 5, and day 28 post enrollment. A subset of

394   participants (n=80) returned for long-term follow-up visits 4-, 7-, and 10-months post

395   enrollment, with peripheral blood obtained. Longitudinal samples from the 56 SARS-CoV-2-

396   infected outpatients who were in the placebo arm of the broader Lambda study were obtained

397   and assessed here.

398   Stanford Favipiravir Cohort (Cohort 2):

399   149 participants were enrolled in a phase 2 randomized controlled trial of Favipiravir beginning

400   July 12, 2020 (NCT04346628). Inclusion/exclusion criteria and the study protocol for the trial

401   are publicly available. Briefly, adults aged 18 – 80 years old were enrolled within 72 hours of a

402   positive NAAT for SARS-CoV-2. Upon enrollment, participants were mildly symptomatic with

403   no evidence of respiratory distress. Participants were randomized to receive favipiravir or

404   placebo. Participants were followed for 28 days, with study visits on days 1, 5, 10, 14, 21 and 28.

405   At each study visit, clinical assessment was performed and oropharyngeal swabs and blood

406   samples were collected. Samples collected upon enrollment from the 69 SARS-CoV-2-infected

407   outpatients who were in the placebo arm of the broader Favipiravir study were obtained and

408   assessed here.

409   Mount Sinai Cohort (Hospitalized COVID-19 patients):

410   Fifty-two samples were obtained from hospitalized COVID-19 patients enrolled in the Mount

411   Sinai Health System (MSHS) collected by the Mount Sinai COVID-19 biobank [22]. The median

412   age was 65 years old with a range from 33 - 98 years old. There are 31 males and 21 females in

413   the study. 13 patients succumbed to disease.

414   Stanford Adult vaccine cohort:

415   Fifty-seven healthy volunteers were enrolled in the study approved by Stanford University

416   Institutional Review Board (IRB 8629). The median age was 36 years old with a range from 19 -

417   79 years old. There are 28 males and 29 females in the study. There are 27 White participants, 23

418   Asian participants, 4 Black participants, 1 Native American participant, and 2 other participants.

419

420   Cell lines. Human embryonic kidney (HEK) 293T (American Type Culture Collection, ATCC;

421   CRL-3216) and Vero (ATCC; CCL-81) cells were grown and maintained in 1X Dulbecco's

422   Modified Eagle Medium (DMEM; ThermoFisher Scientific) supplemented with 10% fetal

423   bovine serum (FBS).

424

425   Cloning, expression, and protein purification. The His_6-tagged SARS-CoV-2 RBD and full-

426   length SARS-CoV-2 spike protein were purified in house as previously described.[3] Briefly, both

427   the constructs were transiently transfected into Expi293F cells (Thermo Fisher Scientific) and

428   proteins purified from culture supernatants Ni-nitriloacetic acid (NTA) resin (GE HealthCare).

429

430   Generation of SARS-CoV-2 pseudoparticles. To generate vesicular stomatitis virus (VSV)

431   pseudotyped with the S of SARS-CoV-2, we first constructed an expression plasmid encoding

432   the Wuhan S. We did this by modifying a pCAGGS mammalian expression vector encoding the

433   full-length Wuhan S and deleting its last 18 amino acids of the cytoplasmic domain, which we

434   call pCAGGS-SΔ18. This reagent was produced under HHSN272201400008C and obtained

435   through BEI Resources, NIAID, NIH: Vector pCAGGS containing the SARS-related

436   coronavirus 2, Wuhan S, NR52310. To generate VSV pseudotyped with SARS-CoV-2 S, we

437   first coated 6-well plates with 0.5 µg/mL poly-D-lysine (ThermoFisher, Cat. No. A3890401) for

438   1 to 2 hours at room temperature (RT). After poly-D-lysine treatment, plates were washed three

439   times with sterile water and then seeded with 1.5e6 cells of HEK 293T per well. After 24 hours

440   (h), cells were transfected with 1 µg of pCAGGS-SΔ18 per well using Lipofectamine 2000

441   transfection reagent (ThermoFisher, Cat. No., 11668019). 48 h after transfection, the cells were

442   washed once with 1X phosphate buffered saline (PBS), and were infected with VSV-ΔG-

443   GFP/nanoluciferase (a generous gift from Matthias J. Schnell) at a multiplicity of infection of 2

444   to 3 in a 300 µL volume. Cells were infected for an hour with intermittent rocking every 15

445   minutes. After infection, the inoculum was carefully removed, and the cell monolayer was

446   washed three times with 1X PBS to remove residual VSV-ΔG-GFP/nanoluciferase. Two mL of

447   infection media (2% FBS, 1% glutamine, 1% sodium pyruvate in 1X DMEM) was added to each

448   well. At 24 h post-infection, the supernatants from all the wells were combined, centrifuged (600

449   *g* for 10 min, 4ºC), and stored at -80ºC until use.

450

451   Neutralization assays. Vero cells were seeded at 5e5 cells per well in 50 μL aliquots in half area

452   Greiner 96-well plates (Greiner Bio-One; Cat. No. 675090) 24 h prior to performing the

453   neutralization assay. On separate U-bottom plates, patient plasma was plated in duplicates and

454   serially 5-fold diluted in infection media (2% FBS, 1% glutamine, 1% sodium pyruvate in 1X

455   DMEM) for a final volume of 28 μL per well. We also included 'virus only' and 'media only'

456   controls. Twenty-five microliters of SARS-CoV-2 pseudo-typed VSV particles (containing 500

457   to 1500 fluorescent forming units) were added to the wells on the dilution plate, not including the

458   "virus-free" column of wells and incubated at 37ºC for 1 hour. Prior to infection, Vero cells were

459   washed twice with 1X PBS and then 50 μL of the incubated pseudo-typed particles and patient

460   plasma mixture was then transferred from the U-bottom 96-well dilution plates onto the Vero

461   cells and placed into an incubator at 37ºC and 5% CO2. At 24 h post-incubation, the number of

462   GFP-expressing cells indicating viral infection were quantified using a Celigo Image Cytometer.

463   We first calculate percent infection based on our 'virus only' controls and then calculate percent

464   inhibition by subtracting the percent infection from 100. A non-linear curve and the half-

465   maximal neutralization titer (pNT_{50}) were generated using GraphPad Prism.

466

467   ELISA. ELISA was performed following a modified version of a protocol described previously3.

468   Briefly, 96 Well Half-Area microplates (Corning (Millipore Sigma)) plates were coated with

469   antigens at 2μg/ml in PBS for 1h at room temperature (RT). Next, the plates were blocked for an

470   hour with 3% non-fat milk in PBS with 0.1% Tween 20 (PBST). All serum samples from

471   patients with COVID-19, and the negative controls were heated at 56°C for 1h, aliquoted and

472   stored at -80°C. Sera were diluted fivefold starting at 1:50 in 1% non-fat milk in PBST. 25μl of

473   the diluted sera was added to each well and incubated for 2h at RT. Following primary

474   incubation with the sera, 25 μl of 1:5000 diluted horse radish peroxidase (HRP) conjugated anti-

475   Human IgG secondary antibody (Southern Biotech) was added and incubated for 1h at RT. The

476   plates were developed by adding 25μl/well of the chromogenic substrate 3,3′,5,5′-

477   tetramethylbenzidine (TMB) solution (Millipore Sigma). The reaction was stopped with 0.2N

478   sulphuric acid (Sigma) and absorbance was measured at 450nm (SPECTRAmax iD3, Molecular

479   Devices). The plates were washed 5 times with PBST between each step and an additional wash

480   with PBS was done before developing the plates. All data were normalized between the same

481   positive and negative controls and the binding AUC has been reported.

482

483   IgG Fc glycan analysis. Methods for relative quantification of Fc glycans and IgG subclasses

484   have been previously described[20,23]. Briefly, IgG were isolated from serum by protein G

485   purification. Antigen-specific IgG were isolated on NHS agarose resin (ThermoFisher; 26196)

486   coupled to the protein of interest. Following tryptic digestion of purified IgG bound to antigen-

487   coated beads, nanoLC-MS/MS analysis for characterization of glycosylation sites was performed

488   on an UltiMate3000 nanoLC (Dionex) coupled with a hybrid triple quadrupole linear ion trap

489   mass spectrometer, the 4000 Q Trap (SCIEX). MS data acquisition was performed using Analyst

490   1.6.1 software (SCIEX) for precursor ion scan triggered information dependent acquisition

491   (IDA) analysis for initial discovery-based identification.

492

493   For quantitative analysis of the glycoforms at the N297 site of IgG1, multiple-reaction

494   monitoring (MRM) analysis for selected target glycopeptides and their glycoforms was applied

495   using the nanoLC-4000 Q Trap platform to the samples which had been digested with trypsin.

496 The m/z of 4-charged ions for all different glycoforms as Q1 and the fragment ion at m/z 366.1

497 as Q3 for each of transition pairs were used for MRM assays. A native IgG tryptic peptide (131-

498 GTLVTVSSASTK-142) with Q1/Q3 transition pair of, 575.9^{+2}/780.4 was used as a reference

499 peptide for normalization. IgG subclass distribution was quantitatively determined by nanoLC-

500 MRM analysis of tryptic peptides following removal of glycans from purified IgG with PNGase

501 F. Here the m/z value of fragment ions for monitoring transition pairs was always larger than that

502 of their precursor ions with multiple charges to enhance the selectivity for unmodified targeted

503 peptides and the reference peptide. All raw MRM data was processed using MultiQuant 2.1.1

504 (SCIEX). All MRM peak areas were automatically integrated and inspected manually. In the

505 case where the automatic peak integration by MultiQuant failed, manual integration was

506 performed using the MultiQuant software.

507

508 Immune cell phenotyping and FcγR quantification. Cryopreserved human PBMCs collected

509 upon enrollment on study day 0 were rapidly thawed, washed, and blocked with Human TruStain

510 FcX (BioLegend) to reduce nonspecific binding. Cells were then stained for viability with

511 Live/Dead Fixable Staining Kit (ThermoFisher) as well as the following antibodies: anti-CD3

512 (clone OKT3), anti-CD11c (clone S-HCL-3), anti-CD14 (clone M5E2), anti-CD16 (clone 3G8),

513 anti-CD19 (clone SJ25C1), anti-CD21 (Bu32), anti-CD27 (clone O323), anti-CD32

514 (STEMCELL Technologies; clone IV.3), anti-CD32B/C (clone S18005H), anti-CD38 (clone

515 S17015A), anti-CD56 (clone 5.1H11), anti-CD138 (clone IA6-2), anti-FucT-VIII (Santa Cruz

516 Biotechnologies; clone B-10), anti-HLA-DR (clone L243) purchased from BioLegend unless

517 noted otherwise. After staining, cells were fixed and acquired using an Attune NxT flow

518 cytometer (Invitrogen). In the case of intracellular anti-FucT-VIII staining, cells were further

519   permeabilized using Intracellular Staining Permeabilization Wash Buffer (BioLegend) prior to

520   acquisition by flow cytometry. Bulk myeloid cells were defined as viable CD3- CD19- CD56-

521   CD11c+ HLA-DR+ cells, while CD16a+ monocytes within this population were additionally

522   positive for CD16a (Fig S3). Within CD16a+ monocytes, non-classical (NC) monocytes were

523   CD16a+ CD14- while intermediate (int) monocytes were CD16a+ CD14+. Leukocyte expression

524   of FcγRs was quantified by measuring the median fluorescence intensity (MFI) of a particular

525   FcγR and comparing it to the MFI of stained Quantum™ Simply Cellular microsphere beads

526   (Bangs Laboratories) of known and discrete antibody-binding capacities. Total CD19+ B cells

527   were similarly assessed from within viable PBMCs. Plasmablasts were further defined as CD19+

528   CD27+ CD38++. Memory B cells were defined as CD19+ CD27+ IgD-, double negative (DN) B

529   cells were CD19+ CD27- IgD-, and naïve B cells were CD19+ CD27- IgD+.

530

531   *In vivo* lung inflammation model. All *in vivo* experiments were performed in compliance with

532   federal laws and institutional guidelines and have been approved by the Stanford University

533   Institutional Animal Care and Use Committee. Polyclonal IgG was isolated from PCR-positive

534   SARS-CoV-2 patients' plasma samples, pooled based on the frequency of afucosylated anti-

535   RBD IgG1 (>20% or <10%). Similarly, plasma from all vaccinated patient samples were pooled

536   and IgG was purified. The purified IgG pools were incubated with SARS-CoV-2 spike trimer at

537   a 20:1 molar ratio overnight at 4°C. Immune complexes were intratracheally administered to 8–

538   12-week-old humanized FcγR or CD16a-deficient mice. Experimental groups were consistently

539   matched for sex and age. 4hr post-administration, mice were sacrificed and bronchoalveolar

540   lavage (BAL) was performed. Immune cells were isolated from within the BAL fluid and stained

541   with the following cell staining panel: Live/Dead Fixable Dye (ThermoFisher), anti-CD2

542   (BioLegend; clone RM2-5), anti-CD3 (BioLegend; clone 17A2), CD11b (BioLegend; clone

543   M1/70), anti-CD45 (BioLegend; clone I3/2.3), anti-human CD64 (BioLegend; clone 10.1), anti-

544   B220 (BioLegend), anti- anti-Ly6G (BioLegend; clone 1A8), anti-MERTK (BioLegend; clone

545   2B10C42), anti-MHC II (BioLegend; clone M5/114.15.2). Once stained, cells were fixed and

546   acquired via an Attune NxT flow cytometer (Invitrogen). Neutrophils were defined as viable

547   Ly6G+ CD11b+ CD3- B220- leukocytes. Monocytes were defined as viable CD11b+ Ly6G-

548   MERTK- MHC IA/IE- CD3- B220- leukocytes (Fig S6). Cell-free BAL fluid was stored at 4°C

549   and processed within 24hr to measure cytokine/chemokine content using a LEGENDplex bead

550   array kit (BioLegend).

551

552   *In vivo* blocking experiments. In chemokine-blockade experiments, mice received intraperitoneal

553   injections of 5mg/kg anti-CXCL1, anti-CCL3, or rat IgG2a isotype control (MAB453,

554   MAB4502, MAB006; R&D) 8hr prior to immune complex administration and immune complex

555   administration and BAL were performed as described above.

556

557   Data and Statistical analysis. The log10+1 transformed half-maximal serum neutralization titers

558   (pNT50) were used to generate the heatmap.

559   Python version 3.8.5 was used for machine learning. The class progressor was mapped to 1 and

560   non-progressor was mapped to 0, making it a binary classification problem.

561   To determine whether the combination of low/no neutralizing antibodies and elevated IgG Fc

562   afucosylation was a predictor of worsening disease trajectory, a logistic regression model was

563   used. The model was trained using data from Cohort 1 (training set), and to obtain the best

564   hyperparameters, GridSearch cross-validation (cv) was performed. The model was tested using

565   an independent test set (Cohort 2) and the ROC AUC score was generated.

566   To generate ROC AUC scores from FcγRs frequency and expression to distinguish progressors

567   and non-progressors, Random Forest Classifier was used. The input data was split using 6-fold

568   cross validation in which the classifier was trained on 5 folds of the data and tested on the

569   remaining part of the data. The ROC response for all these different datasets were used for

570   calculating the mean area under curve.

571   R Studio (version 1.2.1335) was used to perform the multivariate regression analyses and to

572   generate the radar plots and bubble plot using ggplot2 package. For the radar plots, each feature

573   was normalized across the entire dataset and the mean value within each cohort (progressor and

574   non-progressor) was plotted. For the bubble plot, cytokine and chemokine levels were

575   normalized between 0 and the average of all values across all the groups.

576   All other data were analyzed with GraphPad Prism 9.0 software.

606

607   Supplemental information

608   Correspondence and requests for materials should be addressed to T.T.W

609

610 Data availability

611 All raw data are available in the manuscript or from the corresponding author on request.

612 References

613

614 1. M. Z. Tay, C. M. Poh, L. Renia, P. A. MacAry, L. F. P. Ng, The trinity of COVID-19:
615   immunity, inflammation and intervention. *Nat Rev Immunol* 20, 363-374 (2020).
616 2. D. M. Del Valle *et al.*, An inflammatory cytokine signature predicts COVID-19 severity
617   and survival. *Nature medicine* 26, 1636-1643 (2020).
618 3. M. Merad, J. C. Martin, Pathological inflammation in patients with COVID-19: a key
619   role for monocytes and macrophages. *Nat Rev Immunol* 20, 355-362 (2020).
620 4. B. Schurink *et al.*, Viral presence and immunopathology in patients with lethal COVID-
621   19: a prospective autopsy cohort study. *Lancet Microbe* 1, e290-e299 (2020).
622 5. B. J. Barnes *et al.*, Targeting potential drivers of COVID-19: Neutrophil extracellular
623   traps. *J Exp Med* 217, (2020).
624 6. C. Wang *et al.*, Alveolar macrophage dysfunction and cytokine storm in the pathogenesis
625   of two severe COVID-19 patients. *EBioMedicine* 57, 102833 (2020).
626 7. C. Wang *et al.*, Imaging Mass Cytometric Analysis of Postmortem Tissues Reveals
627   Dysregulated Immune Cell and Cytokine Responses in Multiple Organs of COVID-19
628   Patients. *Front Microbiol* 11, 600989 (2020).
629 8. J. S. Warren, P. A. Ward, in *eLS*. pp. 1-9.
630 9. S. Chakraborty *et al.*, Proinflammatory IgG Fc structures in patients with severe COVID-
631   19. *Nature immunology* 22, 67-73 (2021).
632 10. M. D. Larsen *et al.*, Afucosylated IgG characterizes enveloped viral responses and
633   correlates with COVID-19 severity. *Science* 371, (2021).
634 11. W. Hoepel *et al.*, High titers and low fucosylation of early human anti-SARS-CoV-2 IgG
635   promote inflammation by alveolar macrophages. *Sci Transl Med* 13, (2021).
636 12. R. L. Shields *et al.*, Lack of fucose on human IgG1 N-linked oligosaccharide improves
637   binding to human Fcgamma RIII and antibody-dependent cellular toxicity. *The Journal of*
638   *biological chemistry* 277, 26733-26740 (2002).
639 13. D. J. Falconer, G. P. Subedi, A. M. Marcella, A. W. Barb, Antibody Fucosylation Lowers
640   the FcgammaRIIIa/CD16a Affinity by Limiting the Conformations Sampled by the
641   N162-Glycan. *ACS Chem Biol* 13, 2179-2189 (2018).
642 14. P. Smith, D. J. DiLillo, S. Bournazos, F. Li, J. V. Ravetch, Mouse model recapitulating
643   human Fcgamma receptor structural and functional diversity. *Proceedings of the National*
644   *Academy of Sciences of the United States of America* 109, 6181-6186 (2012).
645 15. P. Jagannathan *et al.*, Peginterferon Lambda-1a for treatment of outpatients with
646   uncomplicated COVID-19: a randomized placebo-controlled trial. *Nat Commun* 12, 1967
647   (2021).
648 16. C. Lucas *et al.*, Delayed production of neutralizing antibodies correlates with fatal
649   COVID-19. *Nature medicine*, (2021).
650 17. S. Dispinseri *et al.*, Neutralizing antibody responses to SARS-CoV-2 in symptomatic
651   COVID-19 is persistent and critical for survival. *Nat Commun* 12, 2670 (2021).

18. S. Feng *et al.*, Correlates of protection against symptomatic and asymptomatic SARS-CoV-2 infection. *Nature medicine*, (2021).

19. D. S. Khoury *et al.*, Neutralizing antibody levels are highly predictive of immune protection from symptomatic SARS-CoV-2 infection. *Nature medicine* 27, 1205-1211 (2021).

20. A. W. Charney *et al.*, Sampling the host response to SARS-CoV-2 in hospitals under siege. *Nat Med* 26, 1157-1158 (2020).

21. M. Liao *et al.*, Single-cell landscape of bronchoalveolar immune cells in patients with COVID-19. *Nature medicine* 26, 842-844 (2020).

22. A. F. Rendeiro *et al.*, The spatial landscape of lung pathology during COVID-19 progression. *Nature* 593, 564-569 (2021).

23. P. Brodin, Immune determinants of COVID-19 disease presentation and severity. *Nat Med* 27, 28-33 (2021).

24. Z. Xu *et al.*, Pathological findings of COVID-19 associated with acute respiratory distress syndrome. *Lancet Respir Med* 8, 420-422 (2020).

25. Z. Zhou *et al.*, Heightened Innate Immune Responses in the Respiratory Tract of COVID-19 Patients. *Cell Host Microbe* 27, 883-890 e882 (2020).

26. L. Ziegler-Heitbrock *et al.*, Nomenclature of monocytes and dendritic cells in blood. *Blood* 116, e74-80 (2010).

27. G. D. Thomas *et al.*, Human Blood Monocyte Subsets: A New Gating Strategy Defined Using Cell Surface Markers Identified by Mass Cytometry. *Arterioscler Thromb Vasc Biol* 37, 1548-1558 (2017).

28. T. S. Kapellos *et al.*, Human Monocyte Subsets and Phenotypes in Major Chronic Inflammatory Diseases. *Front Immunol* 10, 2035 (2019).

29. T. T. Wang *et al.*, Anti-HA Glycoforms Drive B Cell Affinity Selection and Determine Influenza Vaccine Efficacy. *Cell* 162, 160-169 (2015).

30. K. V. Sawant *et al.*, Chemokine CXCL1-Mediated Neutrophil Trafficking in the Lung: Role of CXCR2 Activation. *J Innate Immun* 7, 647-658 (2015).

31. J. L. M. Dunn *et al.*, Blocking CXCL1-dependent neutrophil recruitment prevents immune damage and reduces pulmonary bacterial infection after inhalation injury. *Am J Physiol Lung Cell Mol Physiol* 314, L822-L834 (2018).

32. C. Lucas *et al.*, Longitudinal analyses reveal immunological misfiring in severe COVID-19. *Nature* 584, 463-469 (2020).

33. T. S. Rodrigues *et al.*, Inflammasomes are activated in response to SARS-CoV-2 infection and are associated with COVID-19 severity in patients. *J Exp Med* 218, (2021).

34. C. Nathan, Neutrophils and COVID-19: Nots, NETs, and knots. *J Exp Med* 217, (2020).

35. I. Sanchez-Cerrillo *et al.*, COVID-19 severity associates with pulmonary redistribution of CD1c+ DCs and inflammatory transitional and nonclassical monocytes. *The Journal of clinical investigation* 130, 6290-6300 (2020).

36. T. T. Wang, IgG Fc Glycosylation in Human Immunity. *Current topics in microbiology and immunology*, (2019).

37. G. Lauc *et al.*, Genomics meets glycomics-the first GWAS study of human N-Glycome identifies HNF1alpha as a master regulator of plasma protein fucosylation. *PLoS Genet* 6, e1001256 (2010).

38. J. Wang *et al.*, Fc-glycosylation of IgG1 is modulated by B-cell stimuli. *Mol Cell Proteomics* 10, M110 004655 (2011).

698   39.   G. Lauc *et al.*, Loci associated with N-glycosylation of human immunoglobulin G show
699   pleiotropy with autoimmune diseases and haematological cancers. *PLoS Genet* 9,
700   e1003225 (2013).
701   40.   L. Klaric *et al.*, Glycosylation of immunoglobulin G is regulated by a large network of
702   genes pleiotropic with inflammatory diseases. *Sci Adv* 6, eaax0301 (2020).
703   41.   R. Pfeifle *et al.*, Regulation of autoantibody activity by the IL-23-TH17 axis determines
704   the onset of autoimmune disease. *Nature immunology* 18, 104-113 (2017).
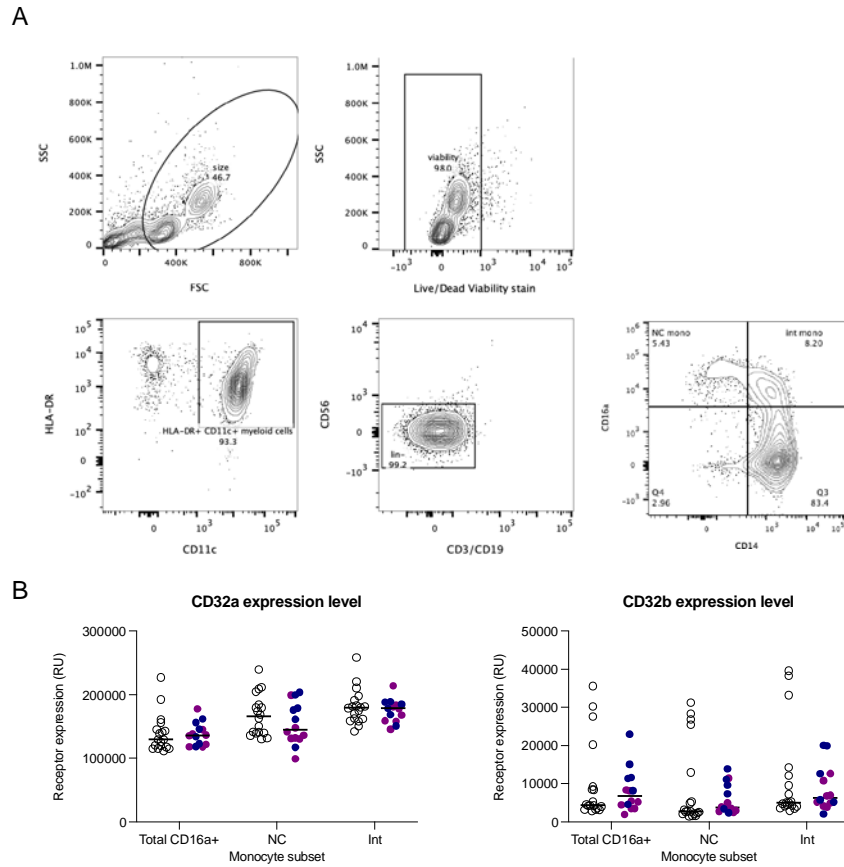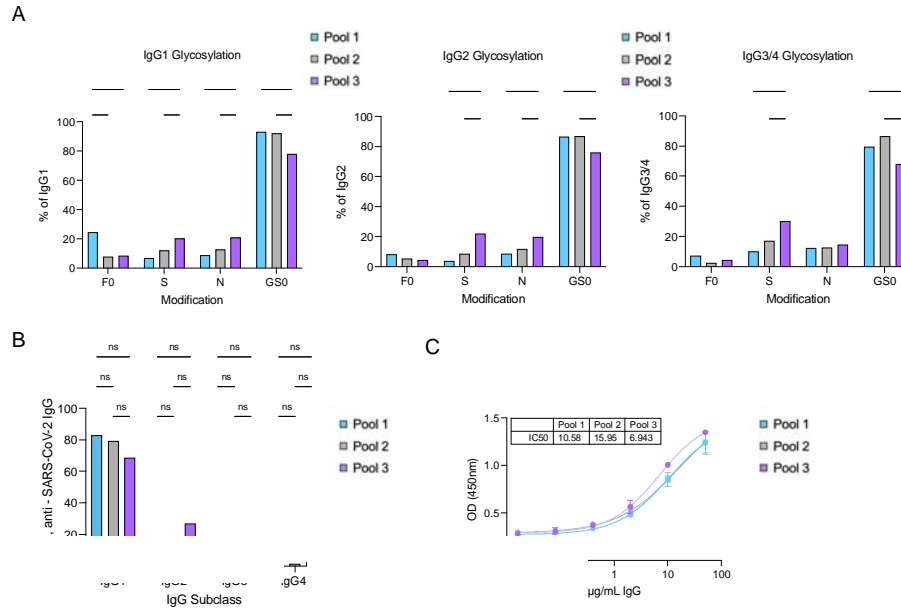
Supplemental Figures

Figure S1
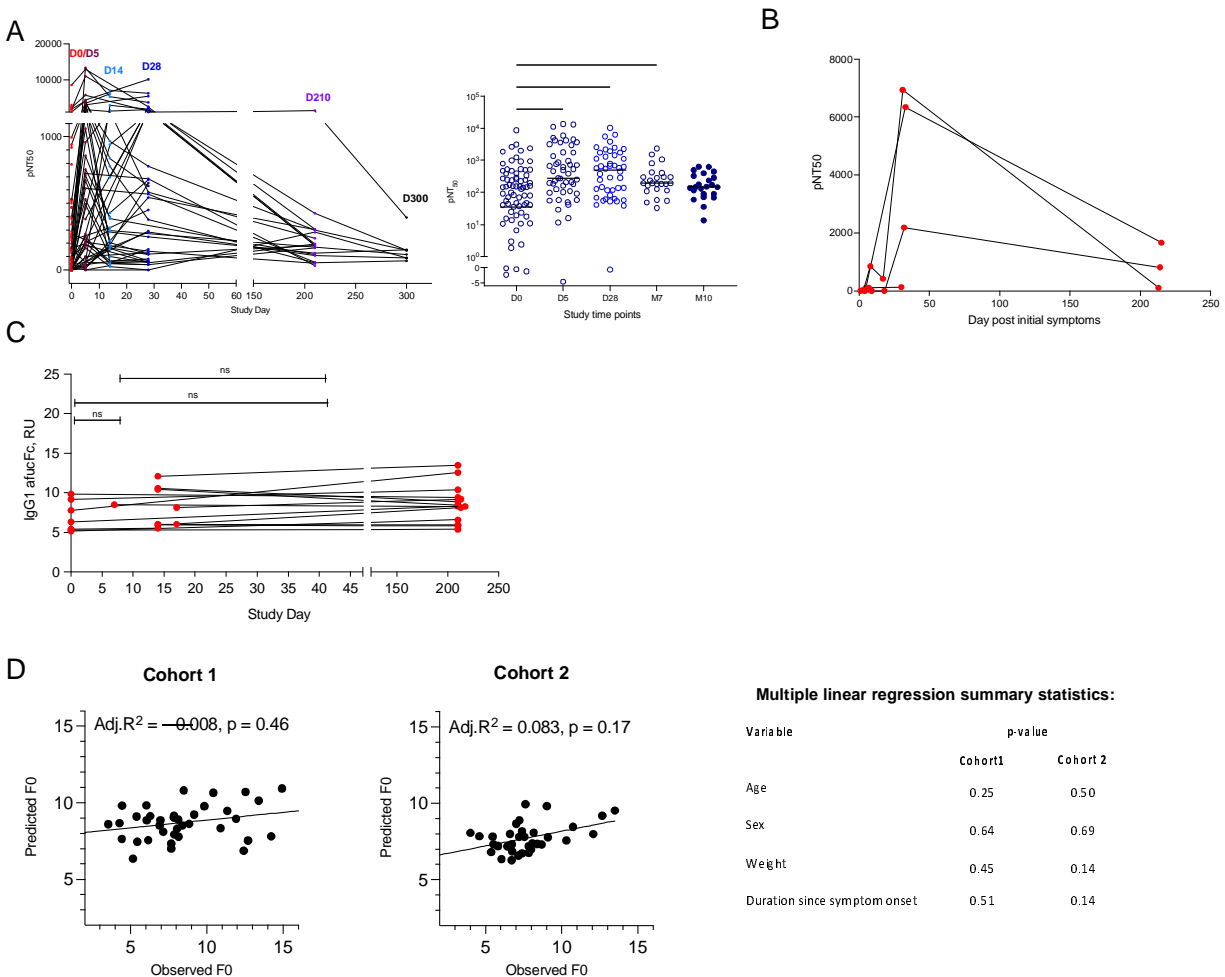
Supplemental Figure S1: **(A)** Half-maximal SARS-CoV-2 pseudovirus neutralizing titers (pNT_{50}) at each study time point. Left panel: graphed to match format of Figure 1A. Right panel: plotted to clearly show the median pNT_{50} at each study time point. **(B)** The kinetics of neutralizing antibody response over time of progressors in Cohort 1. **(C)** Abundance of SARS-CoV-2 specific afucosylated IgG1 in Cohort 1 COVID-19 outpatients over time (n=19). **(D)** Multivariate regression analysis to test the contribution of age, sex, weight, or duration since COVID-19 onset on abundance of afucosylated anti-RBD IgG1 in two cohorts. *$P < 0.05$; **$P < 0.01$; ***$P < 0.001$; ****$P < 0.0001$
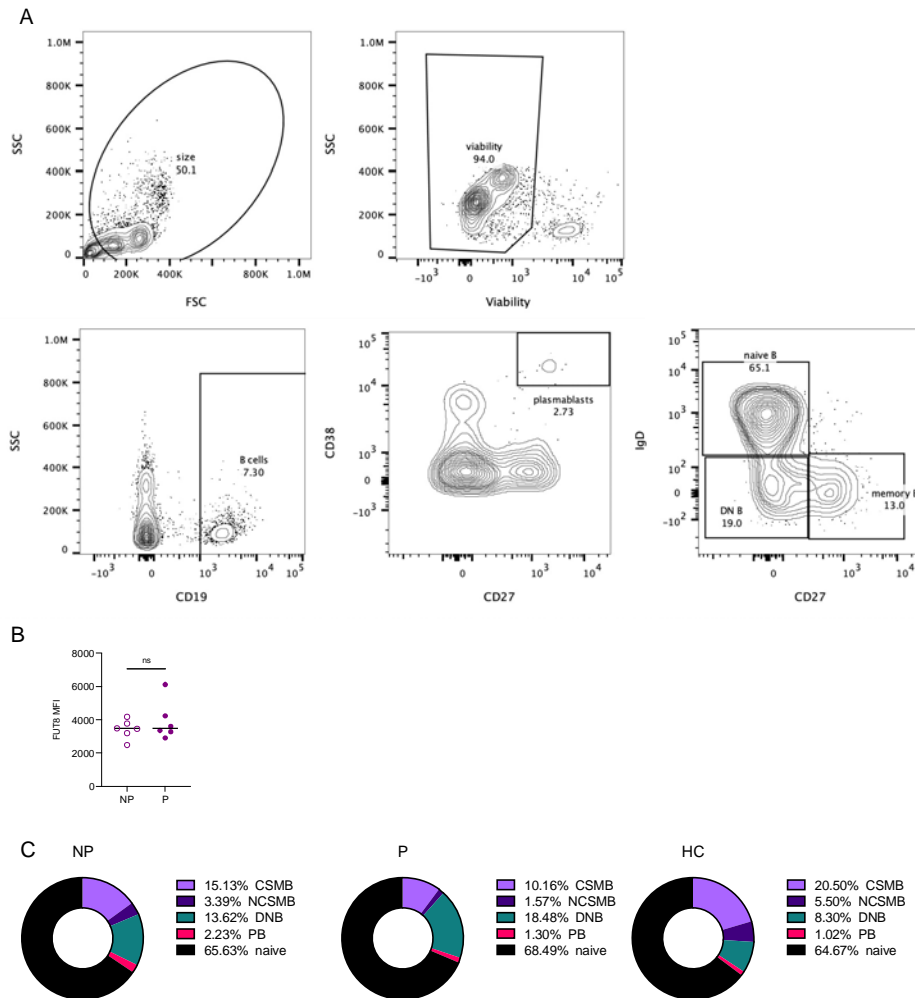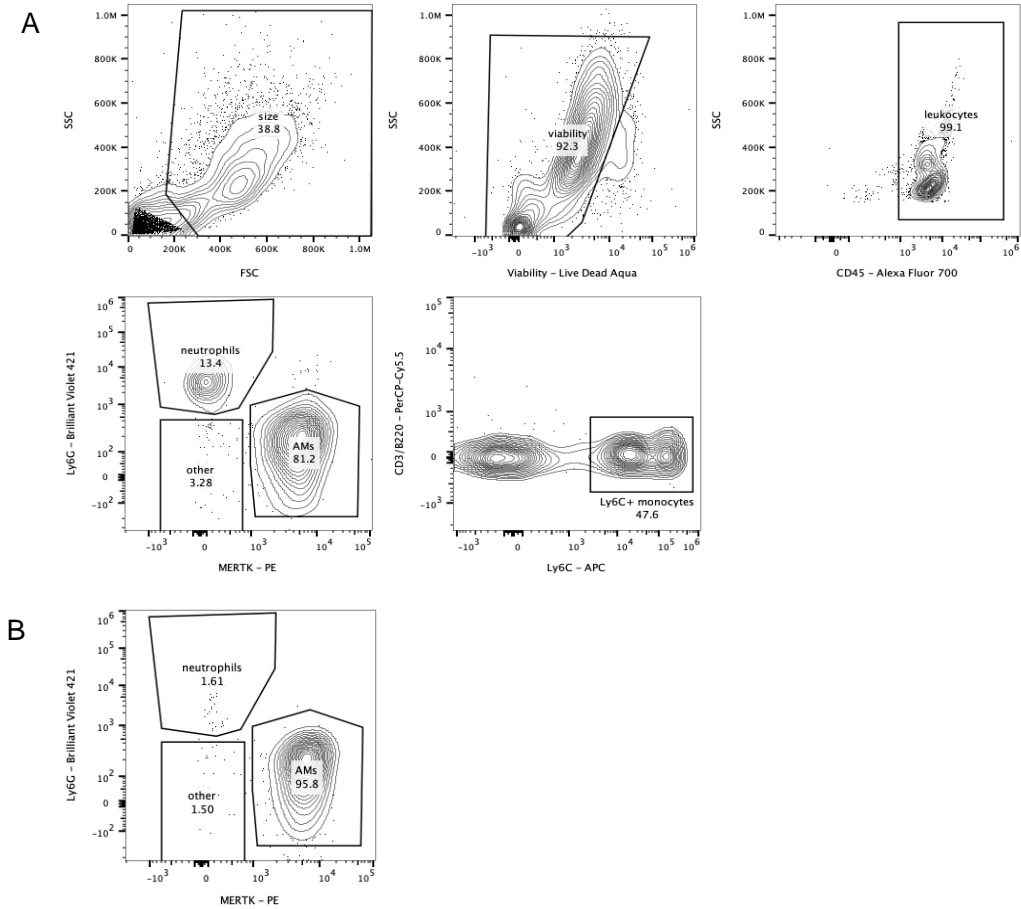
Supplemental Figure S2: (A) Gating strategy for B cell subsets. Total CD19+ B cells were assessed from within viable PBMCs. Plasmablasts were further defined as CD19+ CD27+ CD38++. Memory B cells were defined as CD19+ CD27+ IgD-, double negative (DN) B cells were CD19+ CD27- IgD-, and naïve B cells were CD19+ CD27- IgD+. **(B)** FUT8 expression within total viable PBMCs in progressors (P; n =6) and sex-matched non-progressors (NP; n=6). **(C)** Distribution of B cell subsets (class switched memory B cells (CSMB), non-class switched memory B cells (NCSMB), CD27- IgD- double negative (DNB), plasmablast (PB), and naïve B cells in progressors (P; n = 6), non-progressors (NP, n = 6), and healthy controls (HC, n = 4). P value in (B) was calculated using unpaired Student's t test.

Supplemental Figure S3: (A) Gating strategy for day 0 monocyte subsets and FcγR expression. Bulk myeloid cells were defined as viable CD3- CD19- CD56- CD11c+ HLA-DR+ cells, while CD16a+ monocytes within this population were additionally positive for CD16a. Within CD16a+ monocytes, non-classical (NC) monocytes were CD16a+ CD14- while intermediate (int) monocytes were CD16a+ CD14+. **(B)** FcγR (CD32a and CD32b) expression levels on myeloid cell subsets. P values were determined by unpaired Student's test.

Supplemental Figure S4: (A) Glycan composition (F0-afucosylation, GS0-Galactosylation, S-Sialylation and N-Bisection) of IgG1, IgG2 and IgG3/4 of the individual purified patient IgG comprising polyclonal pool 1 (F0, F0>20%), pool 2 (F, F0<10%), and pool 3 (VAX) polyclonal pools. **(B)** IgG subclass distribution of the individual purified patient IgG comprising polyclonal pool 1, pool 2, and pool 3. **(C)** SARS-CoV-2 full length spike binding of polyclonal pool 1, pool 2, and pool 3. P values in (A-B) were calculated using two-way ANOVA with Šidák's correction. *P < 0.05; **P < 0.01; ***P < 0.001; ****P < 0.0001

Supplemental Figure S5. Gating strategy for immune cell infiltrates in mouse BAL. (**A**) Neutrophils were defined as viable Ly6G+ CD11b+ CD3- B220- leukocytes. Monocytes were defined as viable CD11b+ Ly6G- MERTK- MHC IA/IE-CD3- B220- or Ly6C+ CD11b+ Ly6G- MERTK- MHC IA/IE- CD3- B220- leukocytes. (**B**) Alveolar macrophage were magnetically sorted based on positive expression of MERTK. This sorting method consistently resulted in >90% purity as determined by flow cytometry.

Tables

Table S1. Demographics of the COVID-19 infection cohorts

Stanford Lambda cohort (Cohort 1)	Non-progressor (n=102)	Missing values	Progressor (n=8)	Missing values	p value
Age, years (median, 95%CI)	36 (32.8-38.2)	0	45 (34.4-55.7)	0	ns
Sex Female	45 (44.1%)	0	3 (38%)	0	ns
Race/Ethnicity		0		0	
Latinx	65 (63.7%)		5 (62.5%)		
White	29 (28.4%)		2 (25%)		
Asian	7 (6.9%)		0 (0%)		
Others	1(1%)		1 (12.5%)		
Weight (lbs) (median, 95% CI)	175 (168.1-181.9)	1	198.5 (148.8-248.2)	0	ns
Body mass index (BMI) (median, 95% CI)	27.2 (26.5-28.9)	3	28.8 (23.9-33.7)	0	ns
<25	25 (25.3%)		2 (25%)		
25-30	38 (38.4%)		3 (37.5%)		
>30	36 (36.4%)		3 (37.5%)		
Median days from symptoms onset to study enrollment	4	17	3.5	0	ns
Mean days from symptoms onset to study enrollment	5	17	3.6	0	ns
Median days from randomization to disease resolution	9	0	16	4	ns

Stanford Favipiravir Cohort (Cohort 2)	Non-progressor (n=67)	Missing values	Progressor (n=7)	Missing values	p value
Age, years (median, 95%CI)	40 (36.9-43.1)	0	52 (45.9-58)	0	**
Sex Female	35 (52.2%)	0	3 (42.9%)	0	ns
Race/Ethnicity		4		0	
Latinx	26 (38.8%)		5 (71.4%)		
White	27 (40.2%)		1 (14.3%)		
Asian	7 (10.4%)		0 (0%)		
Others	3(4.5%)		1 (14.3%)		
Weight (lbs) (median, 95% CI)	180 (170.4-189.6)	0	190 (146.5-233.4)	0	ns
Body mass index (BMI) (median, 95% CI)	28.3 (26.8-29.7)	0	30.8 (24.7-37)	0	ns
<25	20 (29.9%)		2 (28.6%)		
25-30	21 (31.3%)		1 (14.3%)		
>30	26(38.8%)		4 (57.1%)		
Median days from symptoms onset to study enrollment	5	3	5	0	ns
Mean days from symptoms onset to study enrollment	5.7	3	6.4	0	ns
Median days from randomization to disease resolution	11	0	16	0	ns

Mount Sinai Cohort	Hospitalized (n=52)				
Age, years (median, 95%CI)	65(60.6-69.4)				
Sex Female	21(40.4%)				
Race/Ethnicity					
Latinx	13 (25%)				
White	7 (13.5%)				
Asian	3 (5.8%)				
Others	29 (55.8%)				
Weight (lbs) (median, 95% CI)	N/A				
Body mass index (BMI) (median, 95% CI)	26.79(24-6-29.01)				
<25	15(28.8%)				
25-30	21(40.4%)				
>30	16(30.8%)				
Median days of sample time point post hospitalization (95% CI)	4(2.87-5.13)				

P values were calculated by comparing features between the progressors and non-progressors using unpaired t-tests with Welch's correction or Fisher's t-test.

Table S2. Description of progressors from Cohort 1

Age	Sex	Days of symptoms prior to enrollment	Days to Hospitalization/ED visit post assessment of mild COVID-19
25	Female	3	0; progressive symptoms leading to hospitalization within 24-hours.
58	Male	4	5; progressively worsening respiratory symptoms. Referred to ED by study-associated physician on study day 5.
44	Female	3	1; progressively worsening respiratory symptoms.
34	Male	2	13; worsening symptoms.
47	Male	5	3; two ED visits within first 3 days for worsening respiratory symptoms.
59	Female	7	0; progressive symptoms leading to hospitalization within 24-hours.
28	Male	4	0; progressive symptoms leading to hospitalization within 24-hours.
46	Male	1	2; progressive symptoms leading to hospitalization.

Table S3. Description of progressors from Cohort 2

Age	Sex	Days of symptoms prior to enrollment	Days to Hospitalization/ED visit post assessment of mild COVID-19
44	Female	8	8; worsening respiratory symptoms
54	Male	2	1; sent by study team to ED for worsening respiratory symptoms and leg swelling, resulted in hospitalization
57	Male	4	2; sent by study team to ED for worsening respiratory symptoms; hospitalized
46	Male	5	3; worsening symptoms and new rash
63	Female	10	5; sent by study team to ED for worsening symptoms
52	Male	4	10; sent by study team to ED for worsening respiratory symptoms; hospitalized
50	Female	8	3; sent by study team to ED for worsening respiratory symptoms; hospitalized

Table S4: Demographics of the Stanford Adult Vaccination Cohort

Characteristics	
Age, years (median, 95%CI)	36(28.3-43.7)
Sex Female	11(64.7%)
Race/Ethnicity	
Latinx	0(0.0%)
White	7(41.2%)
Asian	8(47.1%)
Others	2(11.8%)